Available online at www.sciencedirect.com
SCIENCE DIRECT®
Pergamon
Acta Materialia 51 (2003) 5159–5172
Acta MATERIALIA
www.actamat-journals.com

Some critical experiments on the strain-rate sensitivity of nanocrystalline nickel

R. Schwaiger, B. Moser, M. Dao, N. Chollacoop, S. Suresh *

Department of Materials Science and Engineering, Massachusetts Institute of Technology, 77 Massachusetts Avenue, Cambridge, MA 02139, USA

Received 7 May 2003; accepted 30 June 2003

Abstract

Systematic experiments have been performed to investigate the rate sensitivity of deformation in fully dense nanocrystalline Ni using two different experimental techniques: depth-sensing indentation and tensile testing. Results from both types of tests reveal that the strain-rate sensitivity is a strong function of grain size. Specifically microcrystalline and ultra-fine crystalline pure Ni, with grain size range of >1 μm and 100–1000 nm, respectively, exhibit essentially rate-independent plastic flow over the range 3×10^{-4} to 3×10^{-1} s^{-1}, whereas nanocrystalline pure Ni with a grain size of approximately 40 nm, exhibits marked rate sensitivity over the same range. A simple computational model, predicated on the premise that a rate-sensitive grain-boundary affected zone exists, is shown to explain the observed effect of grain size on the rate-dependent plastic response.

Keywords: Nanoindentation; Tension test; Nickel; Nanocrystalline materials; Strain-rate dependence

1. Introduction

Nanocrystalline materials, with grain size typically smaller than 100 nm, are known to possess some attractive properties, such as high yield and fracture strengths [1–3], improved wear resistance [4,5], and superplasticity at relatively low temperatures [6,7], compared to their microcrystalline counterparts with grain size typically larger than 1 μm. Recently, there has been growing experimental evidence that nanocrystalline materials also exhibit highly strain-rate sensitive mechanical properties [8,9]. However, experimental data available to date in the literature on the strain-rate sensitivity of nanocrystalline metals are very limited, and quantitative results are not conclusive.

Lu et al. [8] studied the effects of strain rate on the tensile flow and fracture behavior of nanocrystalline electrodeposited Cu specimens with a mean grain size of about 30 nm. The strain-to-failure was found to increase significantly with increasing strain rate, which is different from the behavior seen in conventional Cu where the fracture strain decreases slightly at higher strain rates. The flow stress was only mildly dependent on strain rate;

* Corresponding author. Tel.: +1-617-253-3320; fax: +1-617-258-0390.
E-mail addresses: ssuresh@mit.edu (S. Suresh); ruth_s@mit.edu (R. Schwaiger).

1359-6454/$30.00
doi:10.1016/S1359-6454(03)00365-3

within the strain rate range of 6×10^{-5} to 1.8×10^{3} s^{-1} the flow stress at 1% plastic strain increased from about 85 to roughly 150 MPa.

Dalla Torre et al. [9] studied nanocrystalline electrodeposited Ni with a mean grain size of about 20 nm over a wide range of strain rates. Their results partly contradict the results of Lu et al. [8] in that the ductility decreased with increasing strain rate for strain rates ranging from 5.5×10^{-5} to 5.5×10^{-2} s^{-1}. The tensile strength was observed to be approximately 1500 MPa and essentially constant for strain rates between 7×10^{-5} and 5.5×10^{-2} s^{-1}, but increased significantly for strain rates of 10^{1} to 10^{3} s^{-1} to values as high as 2600 MPa. The same trends shifted to slightly higher strain rates were observed on coarser-grained Ni [9]. Wang et al. [10] observed a loading-rate sensitivity in electrodeposited nanocrystalline Ni subjected to tensile and creep tests. Enhanced strain-rate sensitivity at room temperature with decreasing grain size was also found in nanoindentation experiments on nanocrystalline oxides, such as TiO_2 and ZnO [11,12].

Many of the results available in the literature cannot easily be compared. The different techniques used to produce the materials result in widely different internal structures and processing-induced artifacts, such as contamination, porosity, and residual stress. These differences render it difficult to identify the mechanisms responsible for differences in mechanical properties. Another common problem is that only a limited amount of material is typically available to conduct experiments, often with sub-sized specimens. Further, experiments at different strain rates generally involve different specimen designs, loading methods, displacement and strain monitoring techniques, and precision of data. Lu et al. [8] and Dalla Torre et al. [9], for instance, compare results from quasi-static tensile tests with data obtained from high strain rate dynamic loading. Using different instruments, test techniques and loading methods, often requires use of a differently sized specimen [8], which may influence the mechanical response measured [9]. Most theoretical or computational studies, including atomistic simulations [13,14], and continuum-micromechanics based models (e.g. [15,16]), focus on yield strength and related deformation mechanisms, but do not describe the rate-dependent mechanical behavior of nanocrystalline materials under realistic load or strain rates.

There is a critical need for examining the strain-rate sensitivity of nanocrystalline metals and alloys through consistent and systematic data obtained over a wide range of strain rates using a single experimental technique in a fully dense, high purity, and well-characterized material. These results should then be confirmed using a different, independent method on the same materials. Indentation is the preferable method, since the tested volume of material is scaleable with respect to the microstructure. In this manner, strain-rate sensitivity of nanocrystalline (nc), ultra-fine crystalline (ufc), and microcrystalline (mc) specimens of the same material can be studied using a single specimen geometry and loading configuration over a wide strain-rate range where the deformed volume of the material in each case samples a sufficient number of grains for extraction of reliable data. We investigated electrodeposited nc and ufc Ni, which was fully dense and well-characterized. Parallel tensile tests at different loading rates were also performed to verify independently the trend extracted from the indentation experiments. The results from the electrodeposited nc and ufc Ni were compared with conventionally produced mc Ni. In order to provide a rationale for interpreting deformation mechanisms, a simple computational model is proposed. The computational results will be shown to be consistent with both the indentation and tensile experiments.

2. Experimental details

2.1. Materials and specimen preparation

Nickel specimens of different grain sizes were investigated. Fully dense, nanocrystalline Ni sheets were procured from Integran Technologies Inc. (Toronto, Canada). They were produced by electrodeposition and were of 99.8% and 99.9% purity and nominal grain sizes of 20 and 200 nm, respectively. The foils had a thickness of about 150 μm. The electrodeposited materials of nominal 20 and

200 nm grain size will henceforth be denoted as nc and ufc Ni, respectively.

The foils were ground and polished on one side using SiC paper of 500, 1200, 4000 grain size and diamond suspensions of 6, 3, 1, and 0.25 μm grain size. The thickness of the specimens after the polishing procedure was about 100 μm. For comparison, microcrystalline Ni foils of commercial purity were polished following the same procedure. The microstructures of the polished electrodeposited and conventional foils were characterized by Focused Ion Beam (FIB) microscopy (FEI Dual Beam DB 235, FEI, Hillsboro, OR, USA) and optical microscopy, respectively, and by X-ray diffraction (XRD) using Cu–Kα radiation (RU 300, Rigaku International Corporation, Tokyo, Japan).

The specimens used for indentation testing were rectangular with about 10 mm side length. They were glued onto Al cylinders using a standard cyanoacrylate glue ("superglue"). For tensile tests, sub-sized dog-bone specimens were cut from the Ni foils by electrical discharge machining. The width and length of the specimen gage section were 5 and 20 mm, respectively. The shoulder radius was 6 mm and the shoulder width 2 mm. The specimen thickness was equal to the foil thickness.

2.2. Indentation test methods

Two different indenters were used in order to test the electrodeposited Ni foils over a wide range of loads and load or strain rates. This approach also facilitated a comparison of the effects of different indenter designs on the experimental scatter seen for the different grain sizes. The indenters used were: MTS NanoXP system (MTS Systems Corporation, Eden Prairie, MN, USA) for probing the specimens to a depth of 1 μm (maximum load capability: 500 mN, maximum indentation depth: 500 μm), and Micromaterials Microindenter (MicroMaterials Ltd., Wrexham, UK), which is capable of applying loads in the Newton-range, for indenting samples to depths of 3 μm. In all tests, diamond Berkovich tips with a pyramidal tip shape and a tip radius of approximately 150 nm, were used.

The Nanoindenter XP uses a coil-magnet assembly for loading a probe, and measures the displacement into the sample with a capacitance gage. In addition to load and displacement data, the instrument provides continuous measurement of the contact stiffness via a superimposed AC signal during loading [17]. Constant loading rate experiments as well as tests at a constant indentation strain rate [18] can be performed. Details of this instrument can be found elsewhere [17,19].

In our experiments, the specimens were tested at different constant indentation strain rates. The specimens were first loaded to a depth of 1 μm, and the maximum load was held constant for 10 s. Then the specimens were unloaded to 20% of the maximum load and the load was held constant for a period of 60 s while the displacement was monitored to determine the displacement rate produced by thermal expansion in the system. Finally, the load was removed completely. The displacement data were corrected assuming a constant drift rate throughout the test. In all experiments, the contact stiffness was recorded continuously during the loading segment. Indentation strain rates of 0.01, 0.025, and 0.1 s^{-1} were applied. For each strain rate 5 and 10 indents were performed for the nc and ufc Ni, respectively.

The Microindenter is a pendulum-based depth-sensing indentation system with the load applied horizontally through a coil-magnet assembly. The tip displacement is measured with a parallel plate capacitor. The machine is mounted in an enclosure held at a constant temperature to minimize thermal drift effects in the displacement sensing system. Experiments at constant loading rates of 3.8, 12.0, 40.5, and 186.1 mN/s were performed. The loading sequence was as follows: the tip was brought into contact with the material and held there at a load of 100 μN for 60 s while the displacement was monitored. The measured displacement rate was attributed to thermal drift in the system and used to correct the displacement data. Subsequently, the specimen was indented at a constant loading rate to a depth of 3 μm. The load was held constant at its maximum value for 10 s. Finally, the samples were unloaded at the respective loading rates. For each foil and load rate, 10 indents were performed.

The indentation hardness was extracted from indentation data. For the strain-rate controlled

experiments, the hardness was determined continuously throughout the depth of indentation. The results obtained from load-rate controlled indentation were analyzed according to the procedure outlined by Oliver and Pharr [17]. The unloading curves, however, were shifted to the end of the loading segments, in order to compare the hardness at the applied maximum loads. This procedure allows for capturing the influence of load or strain rate on indentation hardness, since creep effects during the hold segment would partially eliminate hardness changes due to the applied strain or load rate. Although this procedure introduces a certain error as the contact stiffness slightly increases during creep due to the depth increase, the hold segment is required to reduce the effect of creep on the unloading curve, particularly at higher load or strain rates [20]. However, we found that the error introduced by this procedure is negligible compared to the experimental scatter. The unloading curves were then fitted with a power law for the data points lying between 20% and 80% of the maximum load.

2.3. Tensile test methods

The trends extracted from indentation tests were verified by using another independent experimental method, i.e. the tensile test. All tensile tests were performed on a computer-controlled hydraulic testing machine (Instron Dynamight, Instron Corporation, Canton, MA, USA) with a load cell capacity of 1 kN. Position-controlled experiments with three different stroke displacement rates were performed. Strain was measured with an extensometer (10 mm gage length) to a maximum strain of 2.5%. The strain data obtained from the extensometer was used to correct the stroke displacement data for machine compliance by comparing the two stress–strain curves in the elastic regime. Since the samples were strained to fracture (strains $>$ 2.5%), the strain derived from the corrected stroke displacement was used for further analysis. The fracture surfaces were investigated by FIB microscopy.

3. Results

3.1. Microstructure

The surface grain structure after polishing is shown in Fig. 1(a) and (b) for nc and ufc Ni, respectively. The nc Ni investigated in this study has been extensively characterized in an earlier study [21], which revealed a narrow grain size distribution with a mean grain size of approximately 40 nm. Growth twins were found to be prevalent.

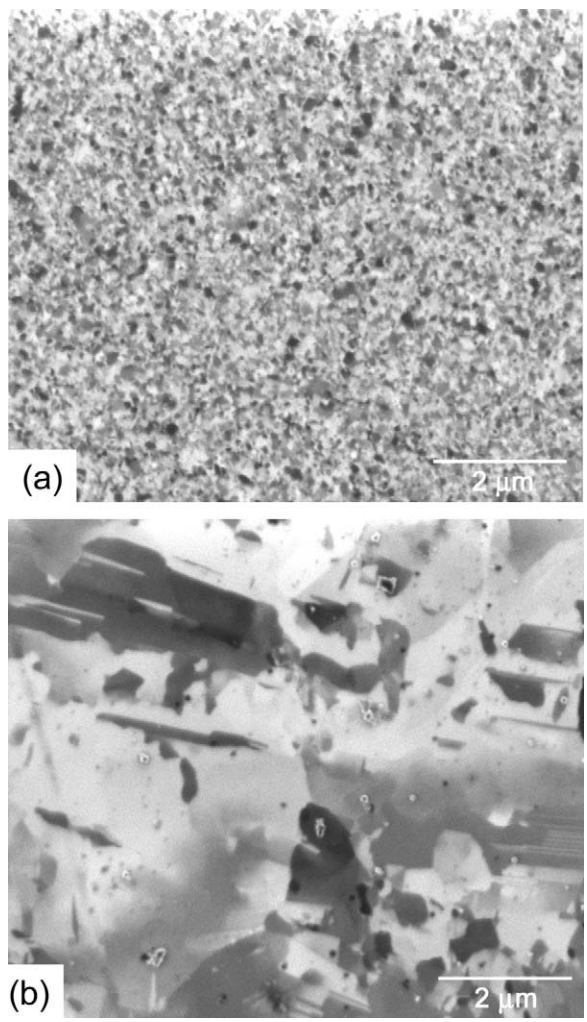

Fig. 1. FIB images showing the grain structure on the surface of the (a) nc and (b) ufc electrodeposited Ni foils after polishing. Due to ion channeling contrast in the FIB, the grain structure is visible.

The grain interior appeared to be clean and devoid of dislocations. The grain boundaries showed no evidence of second phase particles or films. The grain size distribution on the surface of the ufc Ni was not unimodal and a number of grains were significantly larger than the average grain size of 320 nm, which was estimated from quantitative image analysis. The surface grain structure after polishing was more uniform in case of the nc Ni foil. For the mc Ni, a mean grain size of 10 μm was determined by automated image analysis of optical micrographs.

X-ray diffraction involving θ–2θ scans revealed different textures in the three different materials tested. Grains with a ⟨1 1 1⟩-, ⟨1 0 0⟩-, ⟨1 1 0⟩-, or a ⟨3 1 1⟩-orientation perpendicular to the sheet plane were identified. From a comparison of the relative peak heights, the grains in the nc Ni were found to have a preferential orientation in the ⟨1 0 0⟩ and ⟨1 1 1⟩ direction perpendicular to the surface. The ufc Ni had a strong preference for grains with ⟨1 0 0⟩ orientations perpendicular to the surface and a smaller amount of ⟨1 1 0⟩ and ⟨3 1 1⟩ orientations. In contrast, the grains in the mc Ni had, to a large extent, a ⟨1 1 0⟩ and to a smaller extent a ⟨1 0 0⟩ direction perpendicular to the surface.

3.2. Constant strain-rate indentation experiments

Figures 2(a) and (b) show *P*–*h* curves obtained from the ufc and nc specimens, respectively. In both cases three different indentation strain rates were applied. The curves obtained from the ufc Ni show considerable scatter, Fig. 2(a). Within the experimental scatter, no difference between the different indentation strain rates was observed. The *P*–*h* curves given in Fig. 2(b) for the nc material, however, show a distinct and experimentally detectable effect of indentation strain rate. With increasing strain rate, a higher indentation force is required in order to impose the same displacement. The loads applied during the experiments on the nc material were considerably larger than those for the ufc material for a given indenter penetration depth (Fig. 2).

In Fig. 3, the hardness is plotted versus the depth of indentation as determined continuously during

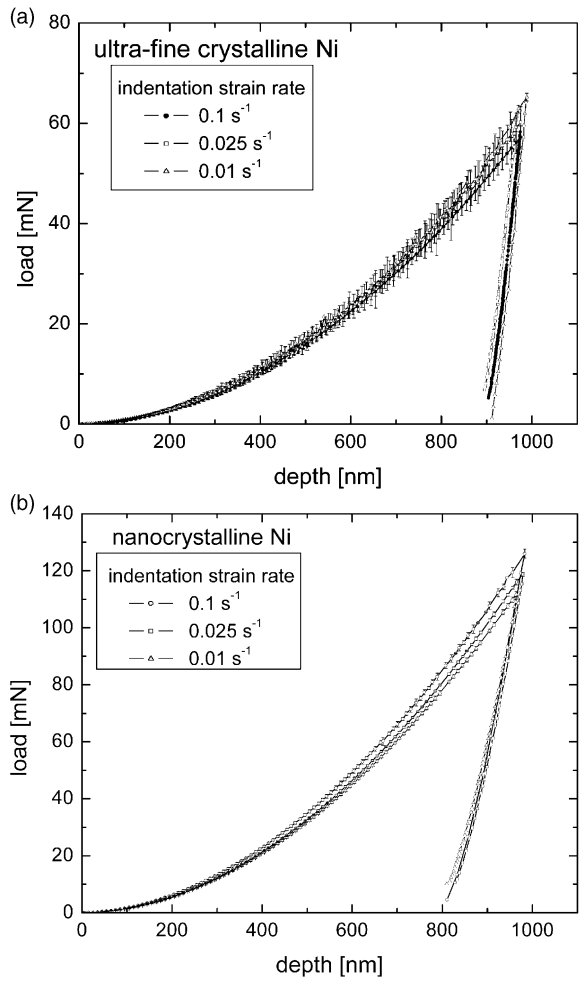

Fig. 2. Load–displacement (*P*–*h*) curves of the (a) ufc Ni (320 nm grain size) and (b) nc Ni (40 nm grain size). The average curve including error bars (95% confidence interval) of 10 and 5 curves, respectively, at three different indentation strain rates is shown.

indentation for both the ufc and nc specimens. The hardness of the nc Ni is significantly higher than that of the ufc Ni. The scatter in the ufc Ni data is considerably larger than in the data obtained from the nc Ni. Within the scatter a clear strain rate effect on the indentation response of the ufc Ni cannot be inferred. In case of the nc Ni, however, the hardness increases with increasing indentation strain rate. The hardness values of the nc Ni are between 5.8 and 6.4 GPa at maximum indentation depth, whereas the hardness of the ufc Ni is

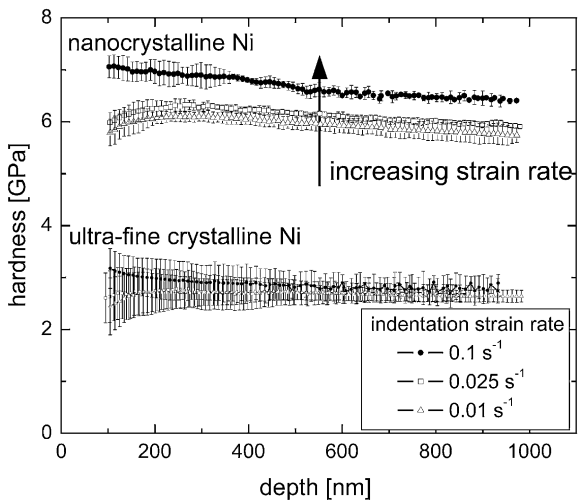

Fig. 3. Hardness versus indentation depth for nc and ufc Ni. The hardness was determined continuously during indentation for three different indentation strain rates. The average of 10 and 5 indents for ufc and nc Ni, respectively, are shown.

almost a factor of two smaller. We attribute the slight hardness decrease of the nc Ni with increasing indentation depth to the compliance of the experimental setup.

3.3. Constant load-rate indentation experiments

The *P–h* curves of the ufc and nc Ni at constant load rates for larger indentation depths are shown in Fig. 4. Four different load rates were applied. The unloading portion of the curves was shifted to the depth achieved at the end of the loading segment. Hardness versus load rate is plotted in Fig. 5 at $h = 2800$ nm. In case of the ufc Ni, the hardness is constant, whereas in case of the nc Ni the hardness increases with increasing load rate.

3.4. Tensile tests

Stress versus strain calculated from the compliance-corrected stroke displacement for $\dot{\varepsilon} = 3\times10\ s^{-1}$ for the different materials tested is shown in Fig. 6(a). Yield strength as well as tensile strength (TS) increase with decreasing grain size. For the mc Ni foil only the beginning of the curve is shown, as fracture occurred at about 30% strain. Figure 6(b) shows stress–strain curves obtained

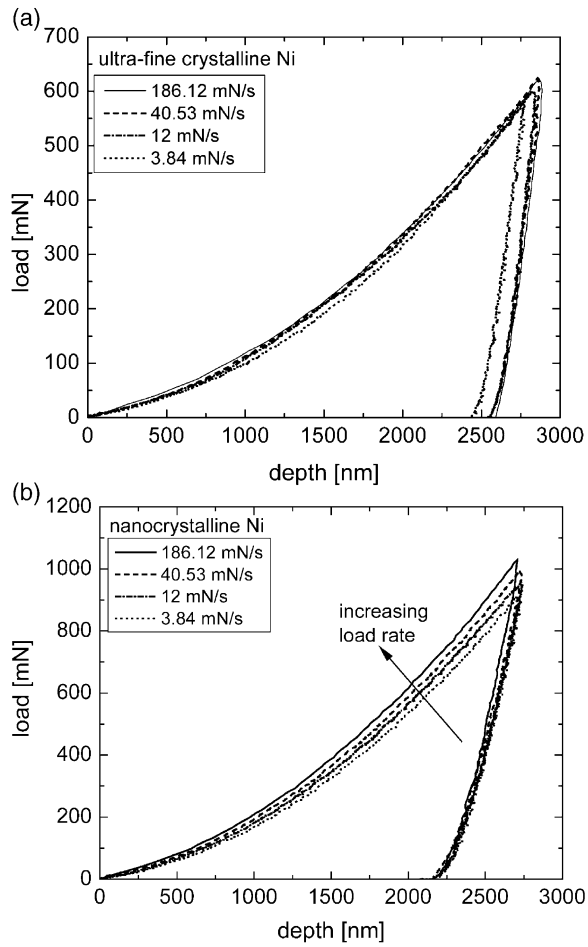

Fig. 4. Load–displacement (*P–h*) curves of the (a) ufc Ni (320 nm grain size) and (b) nc Ni (40 nm grain size). The average curves of 10 and 5 curves, respectively, at four different load rates are shown.

from the nc Ni deformed at three different strain rates. The flow stress increases with increasing strain rate.

3.5. Fracture surfaces

Tensile fracture surfaces of the three different materials are shown in Fig. 7. The mc specimens showed some necking in both directions, in plane and perpendicular to the foil. Necking in the nc and ufc specimens was only observed perpendicular to the foil.

The fracture surfaces of nc, ufc, and mc Ni

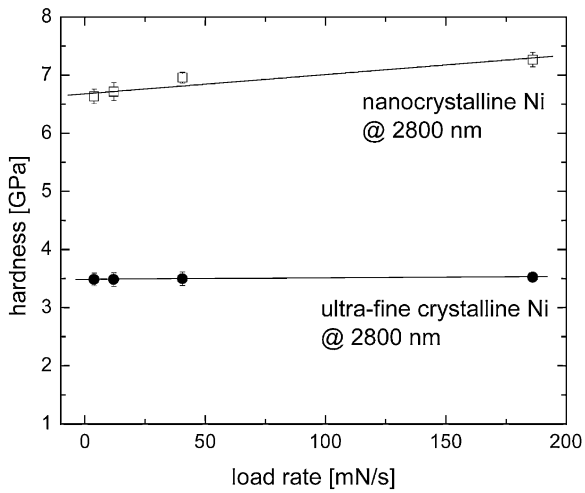

Fig. 5. Hardness versus load rate for nc and ufc Ni at h = 2800 nm. The hardness was determined at the indentation depth at maximum load for four different load rates (3.84, 12.0, 40.53, and 186.12 mN/s). The average of 10 indents for ufc and nc Ni are shown.

specimens, respectively, deformed at a strain rate of 3×10^{-1} s^{-1} are shown in Fig. 7(a), (c), and (e), respectively. In all three cases, we found dimples on the fracture surface. However, the average dimple size varies and is smallest for the nc Ni and largest for the mc Ni. The size distribution of the dimples in the nc Ni is more uniform than in the ufc material.

Fig. 7(b), (d), and (f) shows the fracture surfaces of the three materials tested at 3×10^{-4} s^{-1}. Nanocrystalline Ni exhibits rounded shallow surface features (Fig. 7(b)), whereas wavy surface features can be seen in ufc Ni (Fig. 7(d)). In neither of these micrographs dimples are visible. Furthermore, we found pores in the ufc material (see Fig. 7(d)). The mc Ni specimens exhibited a knife-edge like fracture surface with a few dimples (Fig. 7(f)).

4. Discussion

In both indentation and tensile tests, we consistently observe a strengthening effect due to grain size reduction. The indentation hardness of nc Ni is almost twice as high as the hardness of ufc Ni. In the tensile tests, the TS of the three types of

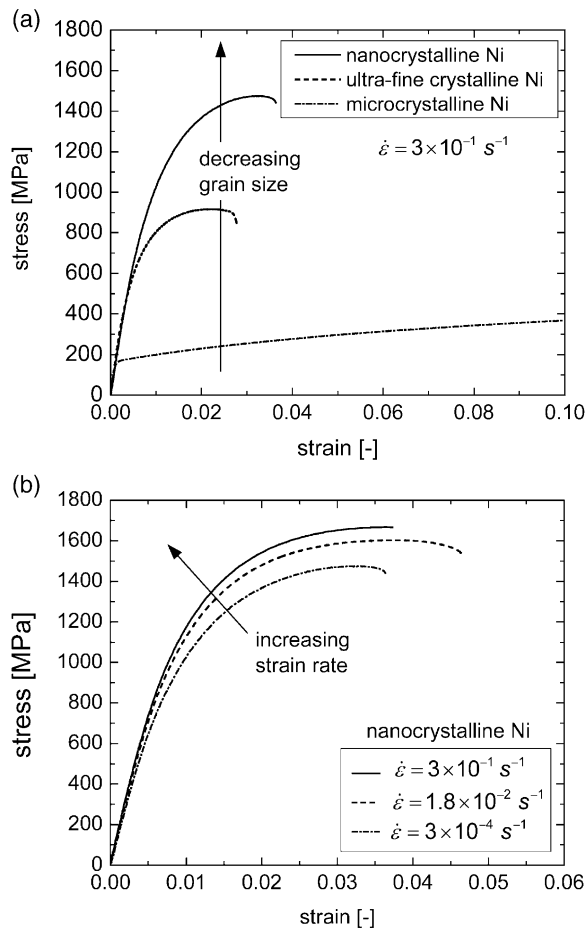

Fig. 6. Stress versus strain (a) for nc, ufc, and mc Ni at a strain rate $\dot{\varepsilon} = 3\times10^{-1}$ s^{-1} and (b) for nc Ni at three different strain rates.

materials tested increased from about 450 MPa for mc (grain size: 10 μm) to about 920 MPa for ufc (grain size: 320 nm) and to more than 1600 MPa for nc Ni (grain size: 40 nm). However, this increase in strength was accompanied by a significant ductility reduction; the strain at TS is reduced from 30% for the mc Ni to only about 2–3% for the nc and the ufc Ni foils. Generally, the strength as well as the hardness values compare well with the values presented by Dalla Torre et al. [9]. However, the overall trends observed in our experiments are different and can be well described by a simple computational model, which is based on recent experimental observations and simulations.

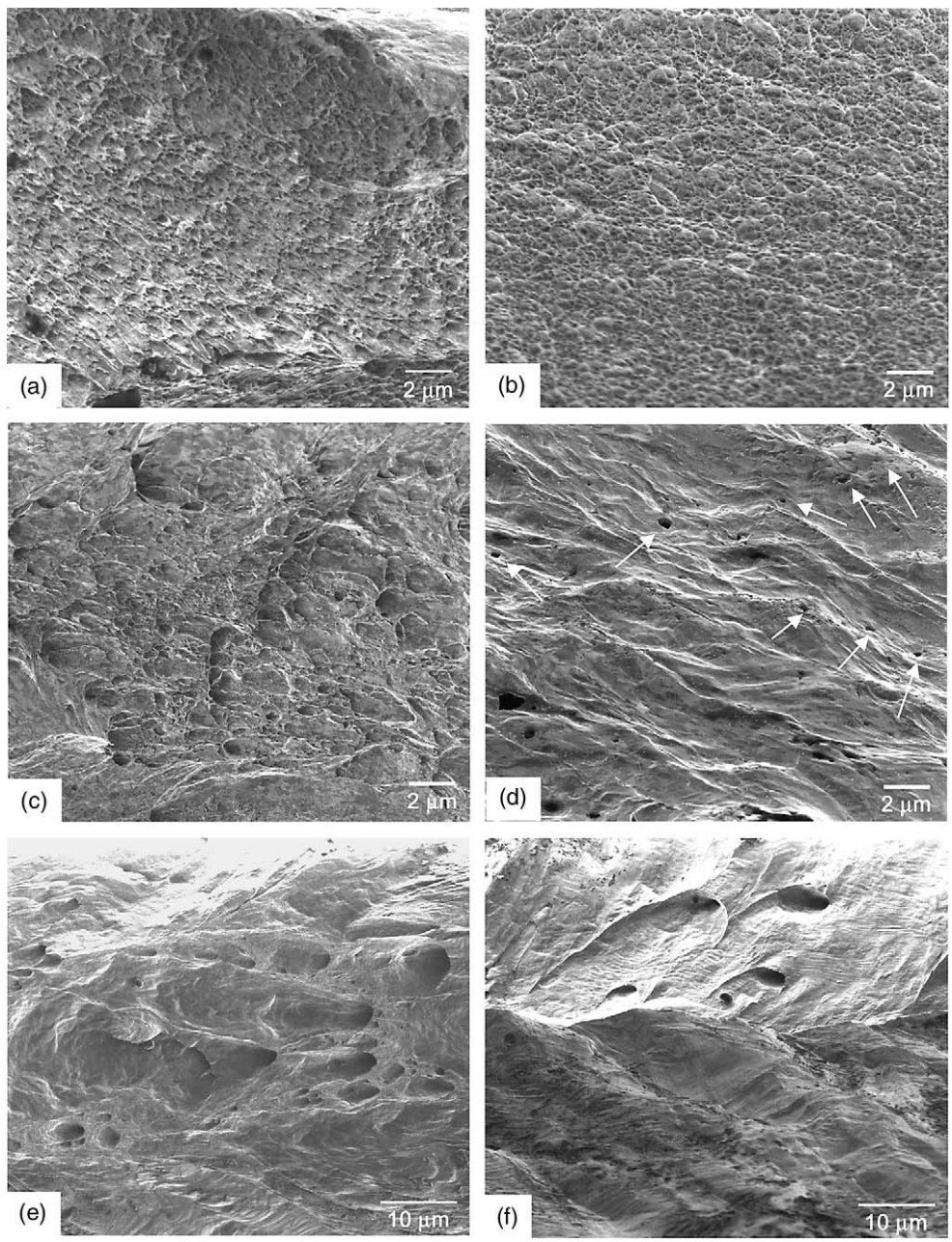

Fig. 7. FIB micrographs of the fracture surfaces for different grain sizes and strain rates. (a) nc Ni, $\dot{\varepsilon} = 3\times10^{-1}$ s^{-1}; (b) nc Ni, $\dot{\varepsilon} = 3\times10^{-4}$ s^{-1}; (c) ufc Ni, $\dot{\varepsilon} = 3\times10^{-1}$ s^{-1}; (d) ufc Ni, $\dot{\varepsilon} = 3\times10^{-4}$ s^{-1}; (e) mc Ni, $\dot{\varepsilon} = 3\times10^{-1}$ s^{-1}; (f) mc Ni, $\dot{\varepsilon} = 3\times10^{-4}$ s^{-1}.

Ex-situ transmission electron microscopy (TEM) studies of nc metals have revealed that grains are essentially dislocation-free [21,22]. The authors argue that the grain boundaries act as dislocation sinks due to image forces. However, during in-situ straining experiments in the TEM dislocation activity in the grain interior has generally been observed for grain sizes larger than 100 nm [23–26].

Kumar et al. [21] performed TEM on the same material investigated in the present study and found that the grain boundaries were atomically sharp and that no amorphous phase was present at the grain-boundary regions, as suggested by Keblinski et al. [27]. High-resolution TEM studies revealed that in electrodeposited nc materials crystallinity is maintained up to the grain boundary [21]. These studies also included in-situ TEM on nc Ni where dislocation activity within grain boundaries was observed at grain sizes as low as 30 nm.

Molecular dynamics simulations of mechanical deformation of nc Cu [13,14] and nc Ni [28] suggest that grain-boundary atoms as well as atoms up to 7–10 lattice parameters away from the grain boundary are heavily involved in plastic deformation. Deformation was mostly found to be taken up by atoms at and nearby grain boundaries. It was further suggested that the material near grain boundaries was easier to deform [13,14] and that the associated deformation mechanisms are likely to be rate-sensitive [13,14]. However, the specific deformation mechanisms have not yet been identified and more investigations are necessary. Here, we propose the concept of a grain-boundary affected zone (GBAZ), which broadly refers to a region adjoining the grain boundaries in nc metals where the crystalline lattice is elastically strained despite the ostensible absence of any point defects. Atoms within this GBAZ are more likely to be involved in the deformation process. However, atomistic simulations are still very limited by the time-scale and consequently the strain-rate sensitivity of nc materials under realistic strain rates has not yet been studied.

In the available continuum-mechanics based models (e.g. [15,16]), the change in mechanical properties as a function of grain size is based on a change in the volume fraction of a grain-boundary phase that is often assumed to be amorphous. A rate-dependent version was developed [29] also assuming a significant volume fraction of an amorphous grain-boundary phase.

Assuming a three-dimensional cubic grain structure, the volume percentage of the GBAZ can be estimated as:

$$\text{GBAZ vol\%} = 100\% - \frac{(d_{GS} - d_{GBAZ})^3}{d_{GS}^3} \quad (1)$$

where d_{GS} is the average grain size, and d_{GBAZ} is the thickness of the GBAZ from the grain boundary. A simple spherical grain model would result in the same equation as Eq. (1). Table 1 lists the estimated volume percentage of the GBAZ in nc and ufc Ni with different grain sizes. Considering a GBAZ of 10 lattice parameters, the volume percentages of GBAZ are estimated to be 44.1 vol% at d_{GS} = 20 nm and 2.6 vol% at d_{GS} = 400 nm.

The following assumptions are made in our model: (i) A GBAZ in a nc or ufc material spans a distance of about 7–10 lattice parameters away from the grain boundary; (ii) the GBAZ is plastically much softer than the grain interior; (iii) the GBAZ deforms with a positive rate sensitivity; (iv) under tensile loading conditions, a strain-based material damage criterion is introduced to model the onset and progression of failure.

A simple power-law type rate-dependent constitutive response is used for the GBAZ:

$$\dot{\varepsilon}_p = \dot{\varepsilon}_0 \left(\frac{\sigma}{\sigma_0} \right)^m \quad (2)$$

where $\dot{\varepsilon}_p$ is the plastic strain rate, $\dot{\varepsilon}_0$ is the reference strain rate, $\sigma_0 = \sigma_0(\varepsilon_e)$ is the effective von Mises stress at the reference strain rate, ε_e is the effective strain, σ is the effective material strength at the current strain rate $\dot{\varepsilon}_p$, and m is the rate sensitivity exponent. Computational parametric studies were

Table 1
Estimation of the volume percentage of the GBAZ

Grain size (nm)	Width of GBAZ (vol%)	
	Ten lattice parameters[a]	Seven lattice parameters[a]
20	44.1	32.6
30	31.3	22.7
40	24.2	17.4
50	19.7	14.1
300	3.5	2.4
400	2.6	1.8

[a] Lattice parameter for Ni: 0.352 nm [30].

performed using a simple linear hardening constitutive behavior for both the grain interior and the GBAZ (see Fig. 8(a)), with the initial yield stress defined by σ_y and a strain-hardening rate defined by θ. For tensile loading conditions, we postulate a simple strain-based failure/damage criterion: the material failure/damage initiates at $\varepsilon_p = \varepsilon_f$, and the material strength drops linearly to a residual strength of σ_r (~0) within an additional strain of $\Delta\varepsilon_f$. The accumulated plastic strain is considered to be decisive for material failure. No damage is introduced when material is deformed under compression, because void formation, the most dominant failure mechanism for the present material [21], is suppressed during compression.

For modeling uniaxial tensile tests of nc Ni, two-dimensional grains of hexagonal shape were separated by a finite border region of GBAZ, as shown schematically in Fig. 8(b). A unit cell model with periodic boundary conditions was used. Different GBAZ volume fractions can be studied by varying the GBAZ depth d_{GBAZ} in relation to the size of the grain interior. Meshes were designed such that the element size was comparable to the typical atomic diameter assuming that the grain size is tens of nanometer. Computational results using two volume fractions of GBAZ, 2% (representing a grain size of 300–400 nm) and 25% (representing a grain size of 30–40 nm), will be presented. About 2500 elements were used in the computations. The material's parameters used in the calculations are summarized in Table 2.

For modeling indentation experiments, the following procedure was adopted. Computational tensile experiments without damage were conducted. The calculated effective tensile stress–strain curves

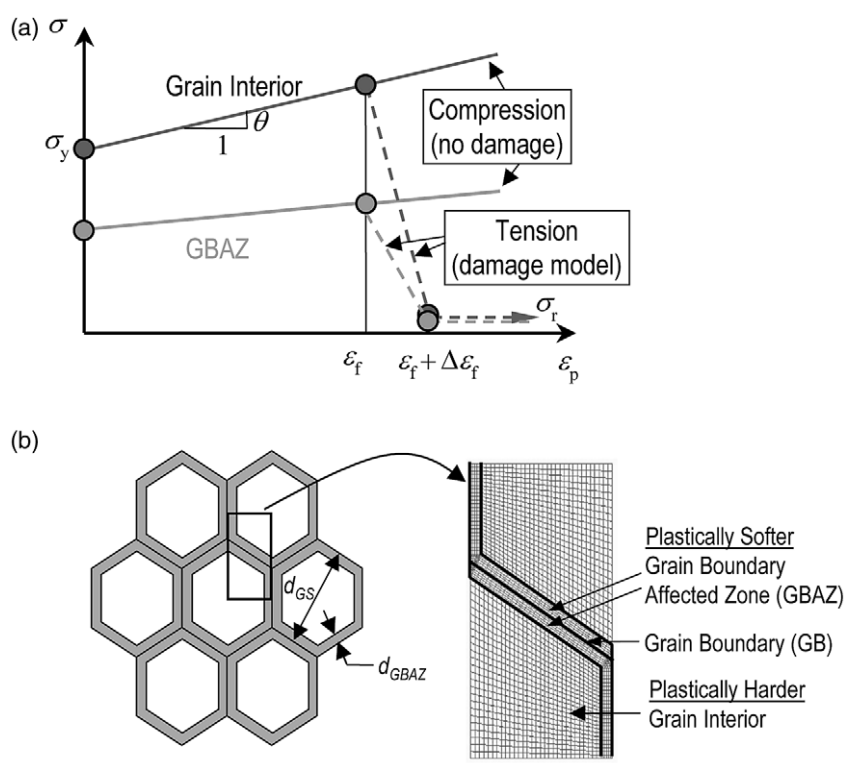

Fig. 8. Schematic showing the computational model. (a) Linear hardening constitutive behavior for both the grain interior and the GBAZ with the initial yield stress σ_y and a strain-hardening rate θ. Material failure/damage under tension is assumed to initiate from $\varepsilon_p = \varepsilon_f$, and the material strength drops linearly to a residual strength of σ_r (~0) within an additional strain of $\Delta\varepsilon_f$. (b) Two-dimensional grains of hexagonal shape separated by the GBAZ preserving crystallinity to the atomically sharp grain boundary. Periodic boundary conditions were applied and a unit cell model was used in all computations.

Table 2
Materials parameters used in the model

	Young's modulus	Poisson's ratio	Initial yield stress	Strain-hardening rate	Rate-sensitivity exponent
Grain interior nc Ni	200 GPa	0.3	2.8 GPa	0	–
Grain interior ufc Ni			0.95 GPa		–
GBAZ			550 MPa		0.03

Local damage initiation strain $\varepsilon_f = 100\%$; damage duration strain $\Delta\varepsilon_f = 1\%$; residual strength $\sigma_r = 1/1000\sigma_y^{GBAZ}$.

at different strain rates were fitted using Eq. (2) in order to extract the material properties, which were used to calculate the load–displacement (*P–h*) response during indentation. Tensile as well as indentation behavior were consequently obtained using the same set of parameters describing the GBAZ and the grain interior. A commercial general-purpose finite element package, ABAQUS (version 6.3, ABAQUS Inc., Pawtucket, RI) was used. A user sub-routine was constructed in order to integrate the rate-sensitive hardening behavior.

Figures 9(a) and (b) show the computational stress–strain curves of ufc Ni and nc Ni, respectively; the results include the TS as well as failure predictions. For the ufc Ni almost no difference can be seen (Fig. 9(a)), whereas in case of the nc Ni, the TS as well as the strain at TS increase significantly with increasing strain rate (Fig. 9(b)). The flow stress and the TS of the ufc Ni can be seen to slightly increase with increasing strain rate, whereas the strain at TS decreased, which is different compared to the nc Ni.

Figures 10(a) and (b) show the predicted indentation curves of nc Ni at different indentation strain and load rates, respectively. The computed results capture the experimentally determined trend and show a similar magnitude of separation between different loading conditions (compare with Figs. 2(b) and 4(b)). Computational indentation results for ufc Ni are not illustrated here and showed vanishingly small differences between different strain rates, which is consistent with the experimental curves shown in Figs. 2(a) and 4(a).

Figure 11 shows the experimental and computational results from tensile tests for the nc and ufc

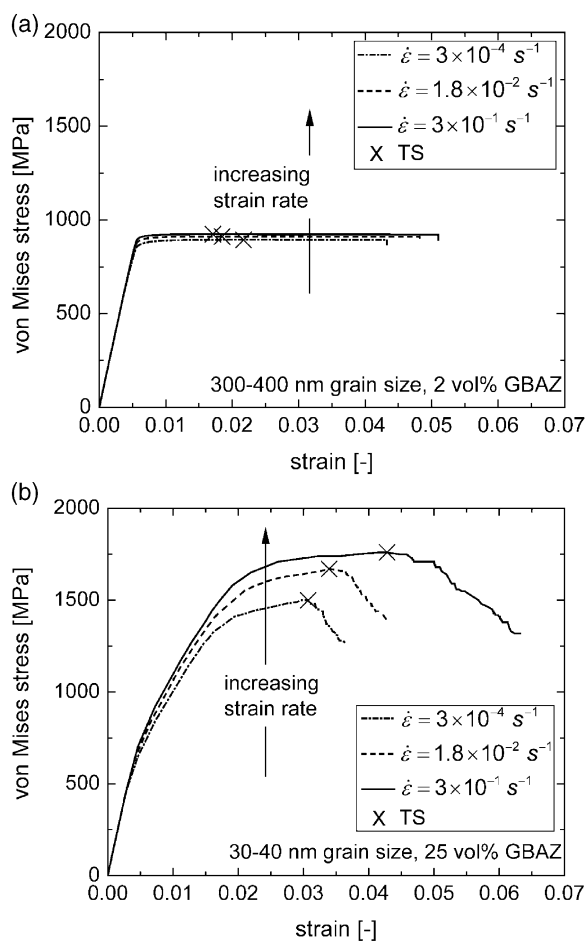

Fig. 9. Computational stress–strain curves at three different strain rates for (a) ufc Ni and (b) nc Ni.

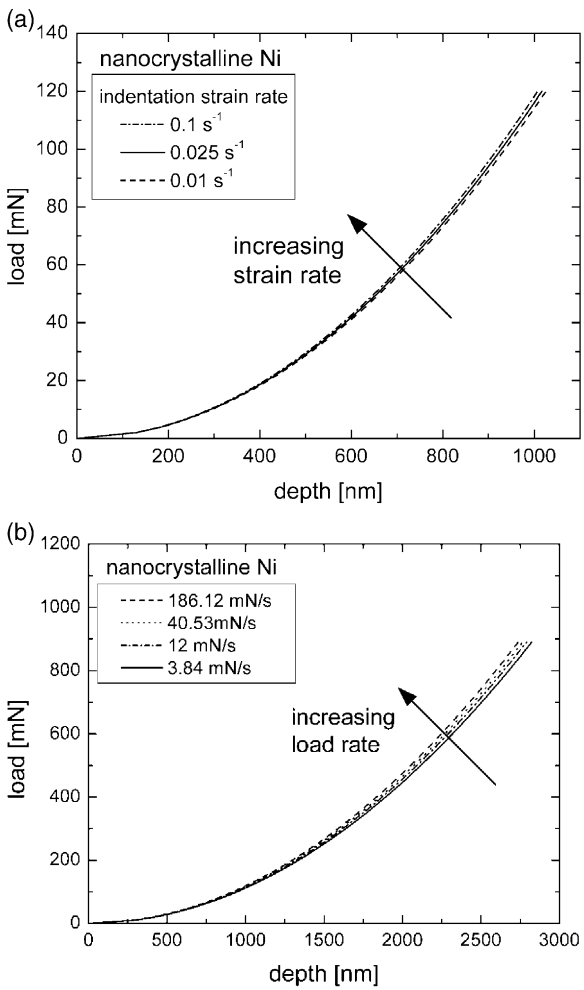

Fig. 10. Computational *P–h* curves for nc Ni obtained at (a) three different indentation strain rates and (b) four different load rates.

Ni. For nc Ni, the offset yield stress at 1% plastic strain (open squares) increases from an average of about 1390 MPa to about 1540 MPa for a strain-rate increase from about 3×10^{-4} s^{-1} to 3×10^{-1} s^{-1}. No such strain rate effect was found in Ref. [9] for the same strain rates, although it has to be noted that the authors evaluated the TS rather than flow stress. Thus, the strength reported in Ref. [9] could be influenced by the onset of necking and therefore not necessarily comparable to the effect on flow stress at 1% plastic strain. In ufc Ni, an increase in flow stress with increasing strain rate

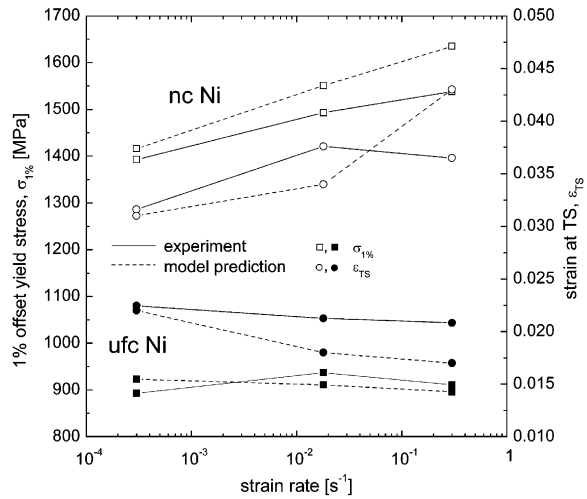

Fig. 11. Comparison of experimental and computational results for tensile tests of nc and ufc Ni. The 1% offset yield stress and the strain at TS are shown versus strain rate.

could not be clearly identified (compare Fig. 11, filled squares). The experimentally found trends are also reflected in the computational results: the 1% offset yield stress is essentially constant in case of ufc Ni and increases with strain rate in case of nc Ni. It is further noted that the absolute values obtained from experiments and computations compare pretty well for the assumptions invoked in the model. Simultaneously, in nc Ni the strain at TS increased by about 0.5% from 3.16% to 3.65% indicating a slight ductility increase (Fig. 11, open circles). A grain size reduction from 320 to 40 nm resulted in an increase in strain at maximum stress from about 2% to more than 3% (Fig. 11), which is consistent with our computational results. In the case of the ufc as well as of the mc Ni tested, we did not observe significant changes of the stress–strain behavior with the applied strain rate within the scatter of the experimental data. Dalla Torre et al. [9] compared the failure strains and observed different behavior. For their nc material, the strains decreased with increasing strain rate. However, in our tests we observed failure strain to be highly defect-sensitive and, hence, not to be sufficiently reliable to determine strain rate effects.

The indentation response of nc Ni is strongly affected by the applied strain or load rates, whereas no such behavior was found for the ufc specimens

(Figs. 2–5). The indentation hardness at 1 μm depth increased from 5.7 GPa at $\dot{\varepsilon}_{ind} = 0.01\ s^{-1}$ to 6.4 GPa at $\dot{\varepsilon}_{ind} = 0.1\ s^{-1}$. A similar trend was observed at higher loads: the hardness increased by almost 10% when the loading rate was increased from 3.8 to 186.1 mN/s. This general behavior could be reasonably well captured by simulating the indentation response using the simple computational model introduced above. As the nc and ufc Ni foils have been produced by the same method, with comparable density and purity, it is likely that the observed rate sensitivity is a consequence of the grain size only. The fact that no strain-rate effect was observed in ufc Ni is not related to the smaller number of grains deformed during indentation. We ensured this by indenting to a depth of 2.8 μm where a significantly larger number of grains have been sampled, and still no such strain-rate effect occurred. However, a potential rate effect in the ufc material may be hidden due to the large scatter in experimental data. In particular, the *P–h* curves to 1 μm depth of the ufc Ni show considerable variations. These variations could be related to the inhomogeneous grain structure at the specimen surface or variations in texture within the sampled volume. Furthermore, a deformation layer at the surface due to mechanical polishing is likely to be responsible for larger scatter. However, neither in the 2.8 μm deep indents nor in the tensile tests, where the influence of the surface is negligible, we found evidence for a strain-rate sensitive deformation behavior. Therefore, we attribute the hardness increase with increasing indentation strain rate in the nc Ni to the small grain size.

It is obvious from our experimental results shown in Figs. 2–6 that the overall plastic deformation of nc Ni is highly rate-sensitive. Due to the lack of dislocation sources, the grain interior of the nc material is expected to deform at stress levels close to the theoretical strength. If the grain interior contributes only little to the overall plastic deformation, the rate-sensitivity observed in nc Ni would be expected to arise from the grain boundaries and the nearby regions, i.e. the GBAZ. Recent molecular dynamics simulations [31] suggest that thermally activated single atomic jumps near the grain boundaries in nc metals play a major role in plastic deformation corroborating the positive strain-rate sensitivity of the GBAZ postulated in our model.

In the literature, conflicting trends of the dependence of failure strain on strain rate have been reported [8,9]. Our computational as well as our experimental results show that in nc Ni the strain at TS increases with increasing strain rate. We emphasize that the computed results represent the material's constitutive behavior assuming uniform deformation "everywhere" in the sample. However, this assumption is not valid beyond TS, since inhomogeneous deformation becomes dominant once necking occurs. Hence, the failure strain is very sensitive to material and sample imperfections. This could be a possible reason for the inconsistent trends reported in the literature.

Under the assumption that the deformation is mainly carried by the GBAZ, the overall ductility of the "composite" nc or ufc material is expected to be limited, even if the GBAZ is ductile (assuming perfectly plastic behavior in the model). This could explain why we observed local but not overall ductility in our nc and ufc samples (see Fig. 7). Two competing factors affect this behavior: (i) the smaller the GBAZ volume fraction, the more limited the ductility, and (ii) the smaller the strength difference between grain interior and GBAZ, the more extended the ductility. Both factors are grain size dependent. The observed fracture surface features shown in Fig. 7 lend support to the basic premise of the computational model that locally ductile failure arises from a strain-controlled process. It is also seen in the experiments that dimple formation is sensitive to strain rate. However, the detailed mechanisms by which the dimple features evolve on the fracture surface are not well understood at this time.

5. Conclusions

- Nanocrystalline pure nickel was found to exhibit a positive strain-rate sensitivity in flow stress, an effect that was not found in ufc and mc nickel. This rate sensitivity was confirmed by two independent experimental methods, namely depth-sensing indentation and tensile testing. The strain-rate sensitivity was observed to be related to the grain size.

- Fractography on tensile specimens revealed a considerable local plastic deformation although macroscopic strain-to-failure is only around 3–4%. A clear difference in fracture surface topography between high and low strain rate testing indicates a transition in deformation mechanism depending on the applied strain rate.
- A simple computational model with a strain-rate sensitive GBAZ that is softer than the grain interior has been introduced. The model, implemented in conjunction with finite element analysis captures the general trends observed in our experiments.

Acknowledgements

This work was supported by the Defense University Research Initiative on Nano Technology (DURINT) on "Damage- and Failure-Resistant Nanostructured and Interfacial Materials" which is funded at the Massachusetts Institute of Technology (MIT) by the Office of Naval Research under grant N00014-01-1-0808. The authors would like to acknowledge use of NanoMechanical Technology Laboratory at MIT and the Nanoindenter XP at the Max-Planck-Institute of Metals Research, Stuttgart, Germany. Thanks are also due to Dr. E. Andrews, Dr. Y.-N. Kwon, and Prof. K.S. Kumar for helpful discussion. R.S. and B.M. acknowledge partial financial support from the DFG (Deutsche Forschungsgemeinschaft) and the SNF (Schweizerischer Nationalfonds), respectively, for their post-doctoral research at MIT.

References

[1] Suryanarayana C. Int Mater Rev 1995;40:41.
[2] Gleiter H. Prog Mater Sci 1989;33:223.
[3] Masumura RA, Hazzledine PM, Pande CS. Acta Mater 1998;46:4527.
[4] Farhat ZN, Ding Y, Northwood DO, Alpas AT. Mater Sci Eng A 1996;206:302.
[5] Jeong DH, Gonzalez F, Palumbo G, Aust KT, Erb U. Scripta Mater 2001;44:493.
[6] McFadden SX, Mishra RS, Valiev RZ, Zhilyaev AP, Mukherjee AK. Nature 1999;398:684.
[7] Lu L, Sui ML, Lu K. Science 2000;287:1463.
[8] Lu L, Li SX, Lu K. Scripta Mater 2001;45:1163.
[9] Torre FD, Van Swygenhoven H, Victoria M. Acta Mater 2002;50:3957.
[10] Wang N, Wang Z, Aust KT, Erb U. Mater Sci Eng A 1997;237:150.
[11] Mayo MJ, Siegel RW, Narayanasamy A, Nix WD. J Mater Res 1990;5:1073.
[12] Mayo MJ, Siegel RW, Liao YX, Nix WD. J Mater Res 1992;7:973.
[13] Yamakov V, Wolf D, Phillpot SR, Gleiter H. Acta Mater 2002;50:61.
[14] Schiotz J, Vegge T, Di-Tolla F-D, Jacobsen K-W. Phys Rev B 1999;60:11971.
[15] Fu H-H, Benson DJ, Meyers MA. Acta Mater 2001;49:2567.
[16] Carsley JE, Ning J, Milligan WW, Hackney SA, Aifantis EC. Nanostruct Mater 1995;5:441.
[17] Oliver WC, Pharr GM. J Mater Res 1992;7:1564.
[18] Lucas BN, Oliver WC. Metall Mater Trans A 1999;30:601.
[19] Pethica JB, Oliver WC. In: Bravman JC, Nix WD, Barnett DM, Smith DA, editors. Thin films: stresses and mechanical properties. Pittsburgh, PA: Materials Research Society; 1989. p. 13.
[20] Feng G, Ngan AHW. J Materials Research 2002;17:660.
[21] Kumar KS, Suresh S, Chisholm MF, Horton JA, Wang P. Acta Mater 2003;51:387.
[22] Ranganathan S, Divakar R, Raghunathan VS. Scripta Mater 2001;44:1169–74.
[23] Ke M, Hackney SA, Milligan WW, Aifantis EC. Nanostruct Mater 1995;5:689.
[24] Hackney SA, Ke M, Milligan WW, Aifantis EC. In: Suryanarayana C, Singh J, Froes FH, editors. Processing and properties of nanocrystalline materials. Warrendale, PA: The Minerals, Metals and Materials Society TMS; 1996, p. 421.
[25] Youngdahl CJ, Hugo RC, Kung H, Weertman JR. In: Farkas D, Kung H, Mayo M, Van Swygenhoven H, Weertman J, editors. Structure and mechanical properties of nanophase materials—theory and computer simulation vs. experiment. Warrendale, PA: Materials Research Society; 2001, p. B1.
[26] Youngdahl CJ, Weertman JR, Hugo RC, Kung HH. Scripta Mater 2001;44:1475.
[27] Keblinski P, Wolf D, Phillpot SR, Gleiter H. Scripta Mater 1999;41:631.
[28] Van Swygenhoven H, Spaczer M, Caro A, Farkas D. Phys Rev B 1999;60:22.
[29] Kim HS, Estrin Y, Bush MB. Acta Mater 2000;48:493.
[30] Cullity BD. Elements of X-ray diffraction. Reading, MA: Addison-Wesley Publishing Company, Inc, 1956.
[31] Van Swygenhoven H, Caro A, Farkas D. Mater Sci Eng A 2001;309-310:440.